Zonal Navier-Stokes Methodology for Flow Simulation about a Complete Aircraft

Jolen Flores* and Neal M. Chaderjian*
NASA Ames Research Center, Moffett Field, California

Transonic Navier-Stokes flow simulations are presented for the F-16A fighter aircraft using a zonal grid approach. This approach subdivides the physical space about the aircraft into an ensemble of simple geometric shapes, thus mitigating many of the difficulties of generating a single grid about a complex shape, e.g., providing adequate grid refinement near all body surfaces to capture the boundary layer. Information is propagated between zones via grid overlapping and a spatial interpolation procedure. Computational C_p compare well with experimental values on the wing, horizontal and vertical tails, fuselage centerline, and the inlet/diverter region. The average y^+ one grid point off the wing is 3. The experimental lift is underpredicted by 2.6%, and the experimental drag is overpredicted by 1.6%. The flexibility of the zonal approach is demonstrated by adding additional zones inside the inlet up to the compressor face to model flow spillage, and downwind of the exhaust nozzle to model power-on conditions. Computations are also presented for the F-16A in sideslip. These results demonstrate that the present zonal approach provides a flexible and viable means of simulating flowfields about complex geometries.

Introduction

THE traditional approach to aircraft design relies heavily upon experimental data to aid the engineer in the design process. Although this approach is very useful, there are some drawbacks. For example, it is very expensive and time consuming to fabricate and test an aircraft model in a wind tunnel.[1] Wind-tunnel interference effects and unrealistic flow conditions can also affect the validity and accuracy of experimental data. It has been anticipated that computational fluid dynamics (CFD) can help alleviate some of these difficulties and will provide information that compliments wind-tunnel data. Some examples where CFD has already been instrumental in improving aircraft design include the Rockwell forward-swept wing,[1] the HIMAT wing,[2], the Airbus A-310,[2] the Lockheed C-141B military transport,[2] and the Cessna Citation III business jet.[3] However, these applications were limited in scope due to the simplicity of the computational geometry or the simplicity of the governing equations.

One long-term goal of CFD has been to simulate viscous flow about a complete aircraft using the Reynolds-averaged, Navier-Stokes equations.[4] However, large amounts of computer time and memory are required to solve this problem due to the numerical stiffness present in Navier-Stokes algorithms and accuracy requirements. This stiffness is further exacerbated in a transonic regime where there are mixed regions of subsonic and supersonic flow with embedded shocks. Yet this flight regime is very important for efficient and cost-effective flight of general aviation jet transports and maneuvering tactical fighters.

In order to address this important goal, CFD has evolved considerably over the past decade by utilizing progressively more complex governing equations and geometries. For example, panel methods based on the linear potential equation are routinely used to simulate inviscid flow about complex aircraft geometries.[5] More recently, however, the Euler equations have also been applied to transonic flow about complete aircraft geometries.[6-12] Technology improvements in supercomputer speed and memory size now provide the opportunity to apply the Reynolds-averaged, Navier-Stokes equations to a complete aircraft. However, three-dimensional grid generation continues to be a pacing item in CFD applications.

Generating a single grid about a complex geometry with appropriate viscous grid clustering near all body surfaces can be a formidable task. A zonal grid approach is one method of circumventing this problem. In this paper, zonal methods refer to the partitioning of the computational space into distinct "zones," each of which is solved with appropriate boundary conditions.

There are several advantages in using a zonal method. First, and most important, it mitigates the difficulty of generating three-dimensional grids for arbitrary complex configurations. One simply subdivides the computational space into an ensemble of simple geometric shapes. Second, zonal methods allow different types of grid topologies to be used in order to improve mesh efficiency. A high mesh efficiency essentially means that more grid points are used on the configuration surface where accuracy is desired, and fewer grid points are wasted in the far field where flow gradients are small. This also provides a straightforward manner of local grid refinement near body surfaces in order to correctly capture viscous gradients. Finally, a zonal method can help alleviate main memory requirements for computers that have large amounts of fast extended storage, e.g., semiconductor memory. This type of computer architecture allows one zone to remain in main memory while other zones reside in extended storage. These zones can be brought into main memory when needed. Zonal grid approaches have been successfully applied to the full-potential equations[13,14] and the Euler equations.[15,16]

Unstructured grids provide another alternative to grid generation about complex geometries. This approach is flexible but was not used here because it typically requires complicated grid point ordering algorithms. Moreover, it is not yet clear how to implement an implicit numerical algorithm on these grids.

The Transonic Navier-Stokes (TNS) code was developed as a proof-of-concept of the present zonal approach. It was also intended to provide benchmark demonstration computations of transonic viscous flow about a complete aircraft. The origi-

Presented as Paper 88-2506 at the AIAA 6th Applied Aerodynamics Conference, Williamsburg, VA, June 6-8, 1988; received Nov. 10, 1988; revision received May 8, 1989.

*Research Scientist, Applied Computational Fluids Branch. Member AIAA.

nal version of the code utilized four zones to simulate transonic viscous flow over low-aspect-ratio wings. Good comparisons with experimental pressure data and separated oil flow patterns were used to calibrate the viscous computations with the zonal concept.[17] The TNS code was then modified into a 16-zone wing-fuselage version and applied to a simplified F-16A fighter aircraft.[18] These simplifications included fairing over the inlet, no empennage, and mounting the aircraft on a sting rather than modeling the exhaust plume. The code was then modified to include the inlet and diverter regions, and good agreement with experimental data was obtained.[19]

In this paper, thin-layer, Reynolds-averaged Navier-Stokes flow simulations for the complete F-16A fighter aircraft are presented using the TNS code. First, zero sideslip flow computations are presented, which utilize 27 and 31 zones. The former extends the modeling of the F-16A geometry to include the horizontal and vertical tails. The latter includes additional grids inside the inlet up to the compressor face to model a different mass flow with spillage and grids extending downwind of the exhaust nozzle to model power-on conditions. Symmetry plane boundary conditions are employed along the centerline of the aircraft. Second, computations are also presented for the F-16A in sideslip. In this flow simulation, the 27-zone grid system is reflected about the symmetry plane to model both sides of the aircraft. This results in a total of 54 zones and 1.3×10^6 grid points.

Governing Equations and Numerical Algorithm

The equations solved in this study are the Reynolds-averaged Navier-Stokes equations written in strong conservation law form. These equations are simplified by using the standard thin-layer approximation for the viscous terms. For zones in which viscous effects are not important, the Euler equations are used. By using the Euler equations over a significant part of the flow domain, the efficiency of the calculation procedure is improved. The governing equations are generally nondimensionalized by freestream quantities and are transformed from the physical domain (x,y,z) to the computational domain (ξ,η,ζ), while retaining the strong conservation law form of the equations.

The original algorithm in the TNS code was an application of the Beam-Warming alternating direction implicit (ADI) scheme[20] due to Pulliam and Steger.[21] The current algorithm used is a diagonal form of this scheme due to Pulliam and Chaussee.[22] The algorithm uses standard second-order-accurate central differencing of the governing equations to construct the appropriate spatial differences. Fourth-order-accurate smoothing operators are included both implicitly and explicitly. Thus, this diagonal form requires the solution of five scalar pentadiagonal matrices along each coordinate direction. A spatially varying time step, which is scaled by the transformation Jacobian, is included to accelerate the steady-state convergence rate. In viscous calculations, the diagonalized algorithm employs an explicit treatment of the viscous terms.[23]

The Baldwin-Lomax algebraic turbulence model[24] is used in the TNS code and has the advantage that it is easy to implement and is computationally efficient. In corner flow zones, e.g., the diverter channel, the thin-layer approximation is used in both directions so that cross-derivative terms are ignored. The turbulence model utilizes a modified length scale in these zones described by Shang et al.[25]

Zonal Philosophy

The F-16A was chosen as a test case of the current zonal methodology for several reasons. First, the geometric complexity would be a challenge for the zonal philosophy. The complexity of this geometry can be seen in Fig. 1 and, in particular, the leading edge of the strake and shelf regions have sharp corners. The engine inlet/diverter region can also be difficult to model. Achieving appropriate clustering at all solid surfaces for this complicated geometry is extremely difficult with a single grid; however, it is a manageable problem when zonal methods are used. Secondly, the ability to simply add zones to model other aspects of the F-16A could be tested, i.e., internal inlet grids up to the compressor face and external nozzle grids to model the exhaust plume.

The TNS solution process begins by generating a base grid about the geometry. The base grid is generated by means of an elliptic method.[26] The base grid is then supplied as input to the zonal code, which subsequently creates 24 zones (by subdividing and refining the original base grid). Through certain parameters in the zonal routine, the zones created are essentially of three types: 1) inviscid zones, 2) viscous zones with clustering on one face for wing or fuselage surfaces, and 3) viscous zones with clustering on two adjacent faces for corner-type flows. For the latter case, the corner-type flow would correspond to the wing-fuselage juncture region. In principle, it is not necessary for all zones to originate from a single base grid. In fact, three additional zones were used to model the inlet/diverter sections, yielding a total of 27 zones with approximately 500,000 grid points. It is also important to realize that a zonal mesh will usually provide greater solution accuracy for a fixed number of grid points than a single grid because more grid points are used in zones near the body and fewer grid points are used in zones away from the body. For example, certain inviscid zones away from the geometry have as few as 5000 grid points, whereas some viscous grids contain as many as 36,000 grid points. For Mach number and angle-of-attack conditions of $M_\infty = 0.9$, $\alpha = 6.0$ deg and Reynolds number based on wing root chord of 4.5×10^6, the viscous clustering yielded an average y^+ value of 3 for the first grid point off the wing surface.

Figure 2 shows the zonal grids for a fuselage/wing cross section. The outer grid is coarse and treated as an inviscid zone.

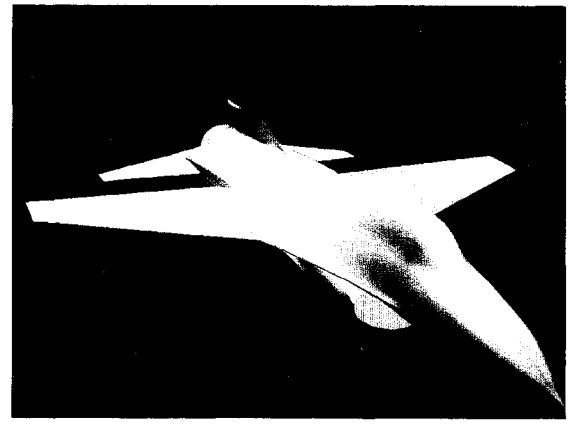

Fig. 1 Surface geometry of the F-16A.

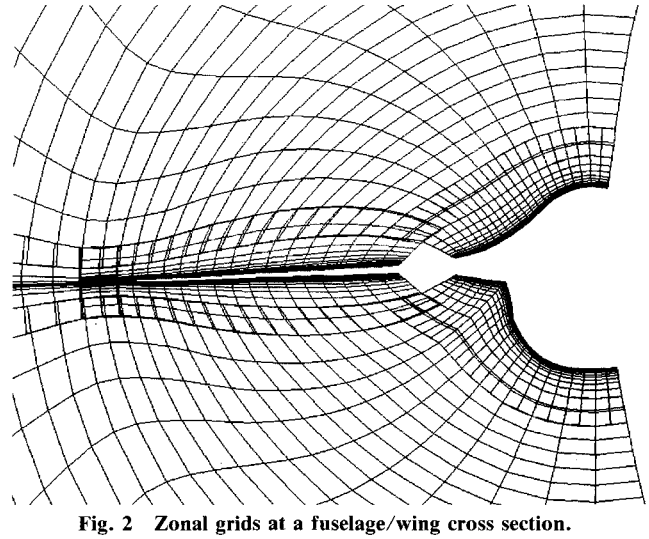

Fig. 2 Zonal grids at a fuselage/wing cross section.

The viscous grids about the fuselage are clustered normal to the surface, and they overlap with the outer inviscid grid. Also illustrated are the viscous zones above and below the wing and the overlap with the outer inviscid zone. Outboard of the wing tip is a special zone that clusters grid points in order to more accurately resolve the tip vortex. An additional viscous zone is also included downwind of the wing trailing edge (not shown in the figure) to model the wing wake region. The wing/fuselage juncture on the upper and lower body surfaces are not shown in this figure.

Figure 3 shows the outline of the zonal grids about the inlet/diverter portion of the F-16A geometry. The grid for the diverter section begins at the same streamwise plane as the face of the inlet and extends back to where the diverter merges into the fuselage body. To reduce modifications required for the zonal routine (as well as the flow solver), it was decided to use two grid zones in the diverter region, an upper diverter grid and a lower diverter grid, each having two no-slip surfaces and a common boundary plane perpendicular to the diverter plate. The beginning of the wedge-shaped inlet grid is on the fuselage underside at a streamwise location near where the strake begins to protrude. This inlet grid extends to the face of the inlet and coincides with the diverter grids at a common vertical boundary plane.

Zonal Boundary Conditions

The zonal boundary conditions in the TNS code fall into two major categories: 1) physical boundaries, e.g., inflow, outflow, and body surfaces, and 2) zonal interface boundaries where zones overlap each other. These two categories are discussed in the following.

In the first category, freestream values are specified at the far-field boundaries, with the exception of the outflow boundary where flow variables are found by zeroth-order extrapolation from the previous plane. The symmetry plane boundary conditions are more complicated: here a zeroth-order space extrapolation is used for the density. A first-order extrapolation is employed for the x- and z-Cartesian velocity components u and w, while the y-Cartesian velocity component v is set equal to zero to force symmetry. Pressure is also found by a first-order extrapolation, and the total energy is computed using the equation of state. At solid surfaces, the no-slip boundary condition is employed for the three velocity components. Surface pressure is found by using the approximation $\partial p/\partial n \approx 0$ such that $p_1 = p_2$, where p_1 is the static pressure on the body surface, and p_2 is the static pressure one grid point off the body surface. The surface density is found from an adiabatic wall assumption that yields $\rho_1 = \rho_2$. Finally, total energy is computed using the equation of state.

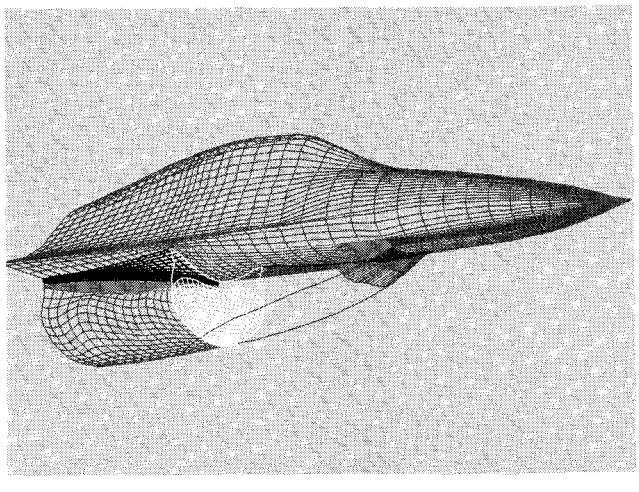

Fig. 3 Wing/fuselage/inlet surface grid with the inlet, upper diverter, and lower diverter grids highlighted.

The second category of boundary conditions has to do with the transfer of data between zones. This is accomplished by means of a spatial interpolation procedure. First of all, the grid zones are carefully (but automatically) constructed to overlap by a specific number of cells (usually one or two). Then, boundary conditions required at the face of one zone are obtained by interpolation from the interior of another zone. This situation is illustrated in Fig. 4. In this hypothetical case, zone 1 is a coarse grid that interfaces with zone 2, a fine grid (see Fig. 4a). Both zones have a common ξ = constant surface (ABCD) as illustrated in Fig. 4b. Note that the coarse grid points are coincident with the fine grid points, so that zone 1 is a subset of zone 2. A simple bilinear interpolation scheme using grid points from zone 1 are used to update the boundary points of zone 2. The process of interpolating information from zone 2 to zone 1, which is required for the ξ = constant surface (EFGH), reduces to direct injection.

The zonal interface boundary conditions described previously are implemented using the most recent information available. This can result in the use of some explicit data at an interface even though the TNS code uses an implicit algorithm. Past experience has shown that explicit boundary conditions do not slow down the convergence rate of an implicit code too much, whereas implicit treatment would require a modification of the implicit matrices. Moreover, the current treatment of the boundaries leads to a simple and flexible scheme. Boundary conditions become a modular element that can be easily changed without modifying the heart of the implicit code. An iterative relaxation procedure at zonal interfaces could also be used to make the boundary treatment more implicit, but this would increase the complexity of the code and the execution time.

Results

Zero Yaw Case

The first computational result presented for the F-16A is for Mach number and angle-of-attack conditions of $M_\infty = 0.9$, $\alpha = 6.0$ deg, and a Reynolds number based on wing root chord

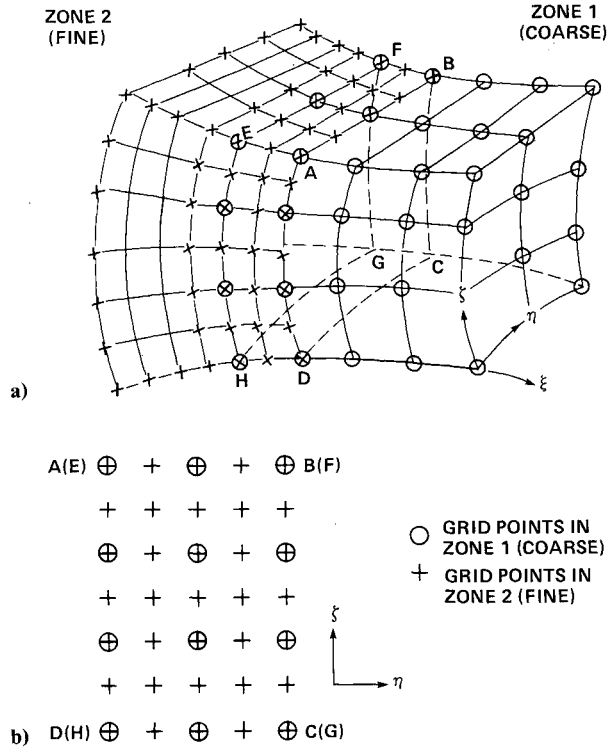

Fig. 4 Sketch illustrating the grid zone interface procedure: a) hypothetical grid-zone interface between a fine grid and a coarse grid; b) planar projection of the ABCD (EFGH) grid-zone interface surface from part a).

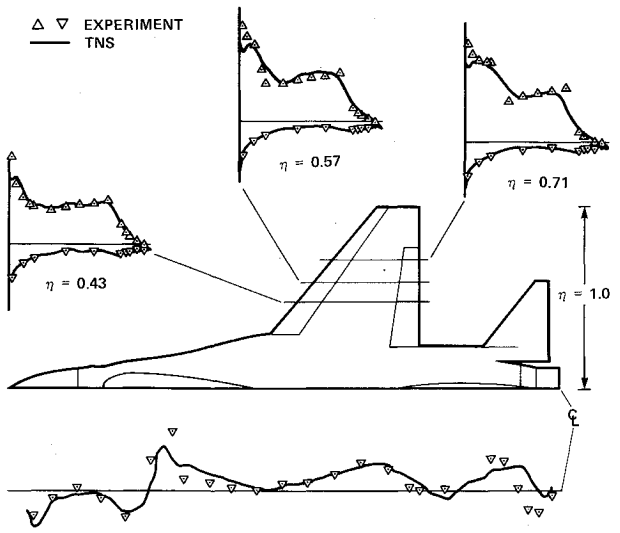

Fig. 5 Comparison of computational and experimental pressure coefficients on the wing and along the centerline of the fuselage for $M_\infty = 0.9$, $\alpha = 6.0$ deg, $Re = 4.5 \times 10^6$.

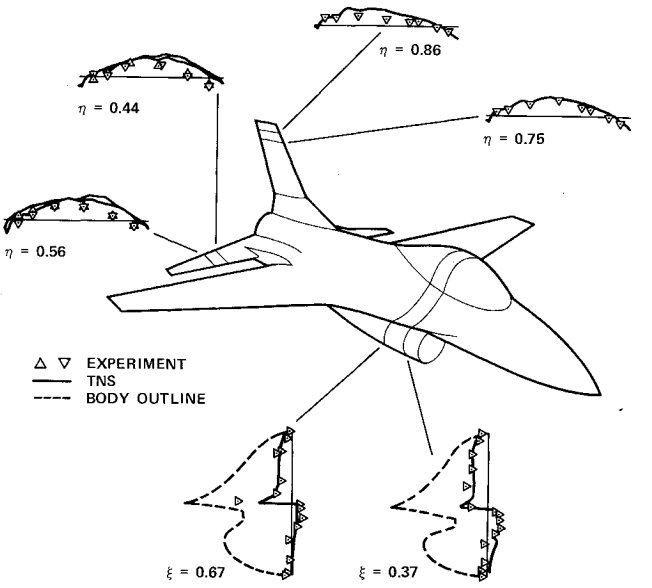

Fig. 6 Comparison of computation and experimental pressure coefficients on the horizontal and vertical tails and two cross-section stations through the inlet/diverter for $M_\infty = 0.9$, $\alpha = 6.0$ deg, $Re = 4.5 \times 10^6$.

of 4.5×10^6. Symmetry plane boundary conditions are imposed along the fuselage centerline, and 27 zones are used to represent the physical space about the half-body geometry.

Figure 5 compares the computational and experimental[27] pressure coefficients at three locations on the wing and along the centerline of the upper fuselage surface. The parameter η indicates the local semispan location, where $\eta = 0.0$ corresponds to the wing root position and $\eta = 1.0$ to the wing tip position. The pressure coefficient comparison along the fuselage centerline begins at the nose of the aircraft and ends at the trailing edge of the horizontal tail. A Mach number correction $\Delta M = 0.02$ is used to improve the comparison of computed shock positions on the wing with experimental ones. This correction is required presumably on the basis of wind-tunnel wall interference effects or perhaps due to a significant streamwise pressure gradient in the tunnel. Without the Mach number correction, the computed shock positions are uniformly upwind of the experimental ones. This correction did not significantly affect the flow solution elsewhere on the aircraft. Unfortunately, there is not enough information in Ref. 27 to assess the effects of the wind-tunnel walls or streamwise pressure gradient on the measured data. With the Mach number correction, the C_p comparison on the wing is good, and the double shock structure is predicted. The C_p "spike" near the leading edge of the wing is due to inadequate grid resolution there. The actual wing has a very small nose radius, while the computational grid represents this as a small "wedge." More grid points are needed to adequately model the leading-edge curvature and capture the proper suction peak. The computed C_p along the top surface of the fuselage centerline compares well with the experiment. Regions of flow compression at the aircraft nose and the front of the canopy are evident, as well as expansion over the fuselage forebody and canopy. A weak shock is also captured on top of the canopy. Downwind of the canopy the flow accelerates and then recompresses due to the influence of the wing. Finally, the flow accelerates along the base of the vertical tail and recompresses downwind of it. The disagreement along the aft portion of the vertical tail occurs because the experimental data are taken inside a small gap that exists between the vertical tail and exhaust nozzle. This gap is not modeled in the computational grid.

Figure 6 compares computational and experimental pressure coefficients on the horizontal tail, the vertical tail, and two cross-sectional body stations through the inlet and diverter. The horizontal and vertical tail C_p are plotted from the local leading edge to the trailing edge (shown left to right), and η is a local spanwise parameter where $\eta = 0.0$ at the root section and $\eta = 1.0$ at the tip. The pressure coefficients at the inlet/diverter cross sections are oriented so that C_p is horizontal (low pressure to the left, high pressure to the right) and plotted against the z-coordinate, which runs vertically from the bottom of the fuselage to the top. The cross-sectional geometry is highlighted by a dashed line. The ξ parameter corresponds to a streamwise position along the fuselage, where $\xi = 0.0$ refers to the cross-sectional plane at the inlet face, and $\xi = 1.0$ to the end of the diverter channel where it blends into the fuselage. The computed horizontal and vertical tail C_p comparisons with their experimental values are fair. The computed C_p for the inlet/diverter cross sections compare reasonably well with experimental data at both streamwise locations. Flow-through boundary conditions are imposed at the inlet face, whereas the experimental data indicate a slight amount of flow spillage there. This accounts for the slight discrepancy along the underside of the inlet at $\xi = 0.37$. There is better agreement with experimental data along the underside of the inlet at $\xi = 0.67$ where the spillage effects are less significant. However, the suction peak around the strake is underpredicted due to inadequate grid resolution in the circumferential direction.

A simulated oil flow pattern near the trailing edge of the horizontal tail is highlighted in Fig. 7. This pattern was obtained by restricting particle traces to a surface one grid point above the aircraft body. Note that the separation line contains node, saddle, and focus critical points.

Regions of separated flow can readily form at many different regions on the aircraft body and significantly affect its aerodynamic performance. This can occur even at low angles of attack due to geometric slope discontinuities or a highly swept wing. Since the location of separated regions are unknown a priori and may be numerous, it is important to use the Navier-Stokes equations to correctly capture these viscous phenomenon.

Figure 8 illustrates the pressure contours on the upper surface of the F-16A, which is modeled by nine zones. The pressure contours are smooth and do not reveal the location of zonal boundaries. For example, one zone ends at a streamwise location just downwind of the canopy and overlaps with the beginning of another zone. High-pressure regions, indicating flow compression, can be seen at the fuselage nose, front of the canopy, and at the leading edge of the vertical tail as expected. Low-pressure regions on the upper surface of the

strake and wing indicate supersonic flow. A λ-type shock can readily be seen on the wing. There is a high-pressure region on the upper surface of the horizontal tail near the root leading edge. This is due to the downwash from the main wing which, even at $\alpha = 6$ deg, creates an effective negative angle of attack at the horizontal tail. Experimental data confirm this phenomenon.

Pressure contours for the underside of the geometry are illustrated in Fig. 9. Again, the smooth blending of contours from the inlet zone to the lower diverter zone in the circumferential direction can be noted. The low pressure on the lower surface of the horizontal tail near the root leading edge indicates that the flow is accelerating from above, i.e., it is experiencing a negative angle of attack.

The computed C_L for the aircraft underpredicts the experimental value by about 2.6%. This is reasonabale because the wing leading-edge suction peak is not adequately captured. The computed C_D overpredicts the experimental C_D by about 1.6%. This drag coefficient agreement is somewhat fortuitous. The slight amount of flow spillage at the inlet face in the experiment indicates a slightly greater discrepancy with the computed drag than indicated previously (since flow-through conditions were used). Moreover, if the computed lift matched the experimental one, this would result in a higher induced drag. Thus, a discrepancy of about 7% between the computational and experimental C_D may be more representative. Over-

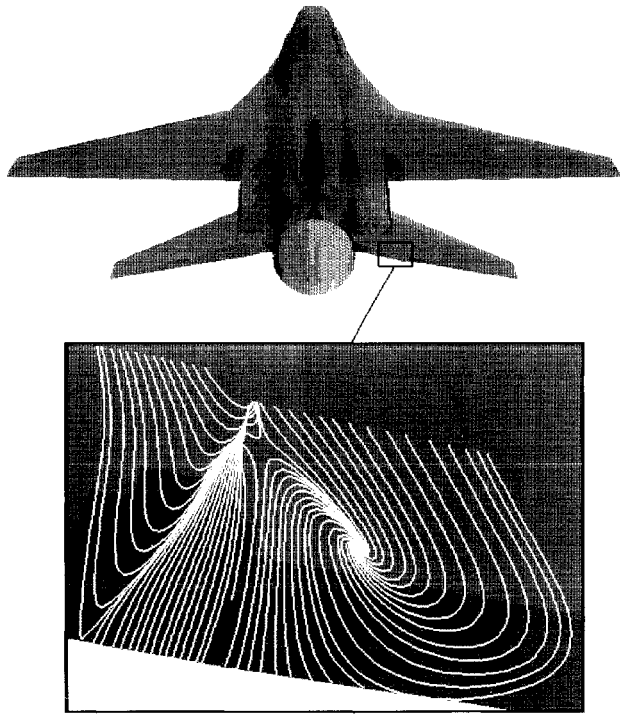

Fig. 7 Simulated oil flow patterns showing flow separation on the aft position of the horizontal tail for $M_\infty = 0.9$, $\alpha = 6.0$ deg, $Re = 4.5 \times 10^6$.

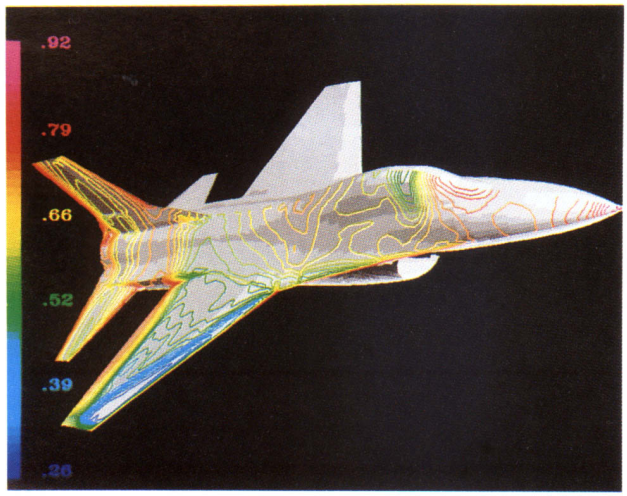

Fig. 8 Pressure contours on the upper surface of the F-16A for $M_\infty = 0.9$, $\alpha = 6.0$ deg, $Re = 4.5 \times 10^6$.

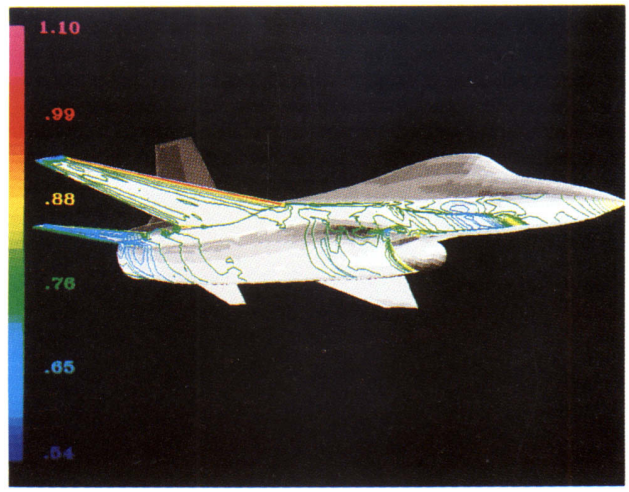

Fig. 9 Pressure contours on the lower surface of the F-16A for $M_\infty = 0.9$, $\alpha = 6.0$ deg, $Re = 4.5 \times 10^6$.

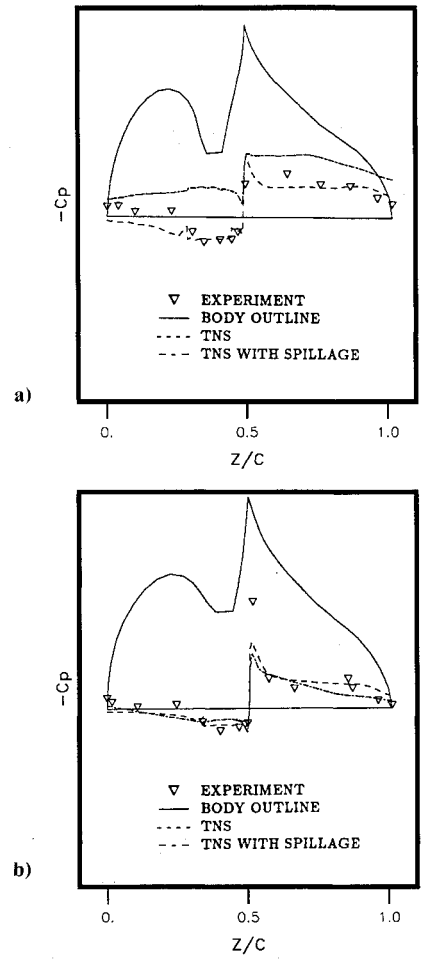

Fig. 10 Comparison of computation and experimental pressure coefficients with and without flow spillage at the inlet face for $M_\infty = 0.9$, $\alpha = 6.0$ deg, $Re = 4.5 \times 10^6$. Cross-section cuts through inlet/diverter/fuselage at a) $\xi = 0.37$, b) $\xi = 0.67$.

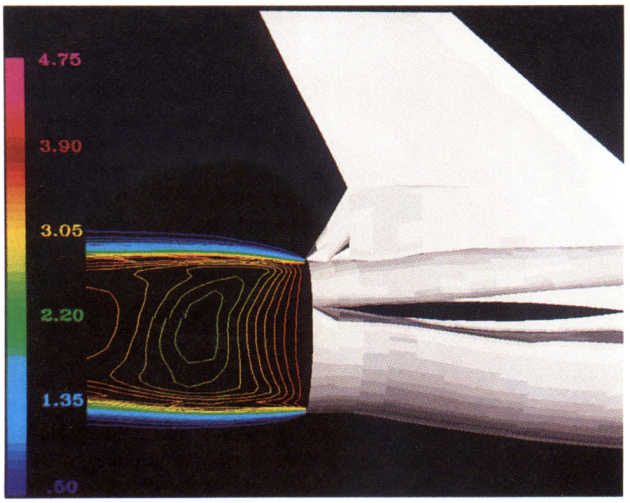

Fig. 11 Computed temperature contours on the symmetry plane of the exhaust plume for $M_\infty = 0.9$, $\alpha = 6.0$ deg, $Re = 4.5 \times 10^6$.

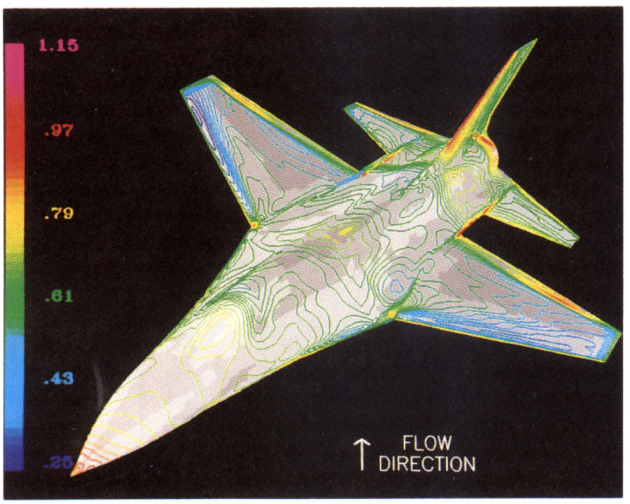

Fig. 12 Computed pressure contours on the upper surface of the F-16A in yaw for $M_\infty = 0.9$, $\alpha = 6.0$ deg, $\beta = 5.0$ deg, $Re = 4.5 \times 10^6$.

all, this is a good agreement that can be improved with grid refinement.

The previous computation was performed on a supercomputer with a 9.5 ns clock cycle time. The TNS code ran at 48 MFLOPS and had a data processing rate of DPR = 38μs/grid point/iteration. This case took approximately 4500 iterations to lower the initial L_2-norm three orders of magnitude in all zones. This required about 25 h of CPU time for a 525,000 point mesh. One could optimize the choice of time steps in different zones and reduce the time required for a solution; however, very conservative time steps were used due to the developmental nature of this computation.

The capability to sequentially add zones as needed can be very useful in a design environment. In order to demonstrate the flexibility of the zonal philosophy, additional grids are added to model the flow inside the inlet and downwind of the exhaust nozzle. This provides the opportunity to control the mass flow rate at the inlet and simulate power-on conditions at the exhaust nozzle. Two grids are added within the inlet (upper and lower grids) and extend internally from the inlet face to the compressor face. These grids are clustered near internal body walls (similar to the diverter grids) to properly capture turbulent viscous flow gradients. Two grids are also added aft of the exhaust nozzle (upper and lower grids) and extend from the exhaust nozzle plane to the far field. These nozzle grids replace the tail sting in the previous computation and overlap with adjacent grids. There are now 31 zones totaling about 550,000 grid points.

Figure 10 compares computed and experimental pressure coefficients at two different cross-sectional planes: a) $\xi = 0.37$, b) $\xi = 0.67$) for the flow-through inlet case (27 zones) and the flow spillage case (31 zones). The solid line outlines the body cross section, which is tilted on its side. The vertical axis is C_p, and the horizontal axis is the local normalized height ($z/c = 0.0$ at the fuselage bottom and $z/c = 1.0$ at the top). The boundary conditions at the compressor face (31 zones) are specified by assuming an isentropic compression within the inlet diffuser. Thus, for a given freestream Mach number, the density and energy values are determined. The velocity components are specified by taking 50% of the upwind-extrapolated values. This percentage is arbitrarily chosen for demonstration purposes in order to create spillage at the inlet. Different percentages will produce different mass flows. In an actual design problem, one would use boundary conditions given by the aircraft engine manufacturer. In Fig. 10a ($\xi = 0.37$), the boundary conditions described above create a much larger amount of spillage at the inlet face than the experiment. This created a large flow expansion around the inlet lip that shifts the C_p curve up. Figure 10b ($\xi = 0.67$) corresponds to a cross section farther downwind of the inlet. The spillage effects are greatly reduced there.

Figure 11 shows static temperature contours that emanate from the nozzle exit plane. A nozzle exit to freestream pressure ratio of 2 is specified, as well as a nozzle exit to freestream temperature ratio of 5. The nozzle exit plane Mach number is specified to be 1. Again, these values were chosen merely for demonstration purposes. At Mach numbers near 1, the characteristics formed are essentially vertical expansion waves that immediately expand the flow. (This is evident by the rapid drop in temperature.) Downwind of the expansion fan, a compression wave system develops due to the reflection of characteristics off the plume boundary. Focusing on the plume boundaries, it can be noted that the upper and lower boundaries both have a smooth transition of temperature. The lower plume boundary is slightly displaced due to angle-of-attack effects. There is a slight mismatch of a few temperature contours in the middle of the exhaust plume. This occurs at a zonal boundary. However, this is a result of the plotting program. Careful examination of the flow variables at this interface indicate that they are identical, as required.

Yaw Case

The simulation of nonsymmetric flow for a yawed F-16A is now presented with $M_\infty = 0.9$, $\alpha = 6.0$ deg, and sideslip angle $\beta = 5.0$ deg. This is accomplished by reflecting the grid system about the symmetry plane and replacing symmetry plane boundary conditions with overlapping or averaging at the fuselage centerline. The 27-zone version of the code is used, i.e., no internal inlet and nozzle zones, resulting in a total of 54 zones. Figure 12 shows the pressure contours on the upper surface of the aircraft. The freestream air is approaching the fuselage from the right side (when facing the aircraft). High-pressure regions can be seen on the vertical tail and the shelf on the windward side of the geometry. Low-pressure regions can be identified on the aft portion of the canopy on the leeward side, indicating accelerated flow across the fuselage centerline. Low-pressure regions are also evident near the leading edge of the wings. The lift of the windward wing is greater than the leeward wing as expected, due to the different sweep angles. A stronger shock also forms near the trailing edge of the windward wing than the leeward wing.

Figure 13 shows unrestricted particle traces that are released at a cross-sectional location just downstream of the nose. Particles released on the windward side are colored in red; the leeward particles are colored in blue. The effects of yaw are clearly seen. The particle traces released from the leeward side are displaced by the canopy and proceed along the fuselage

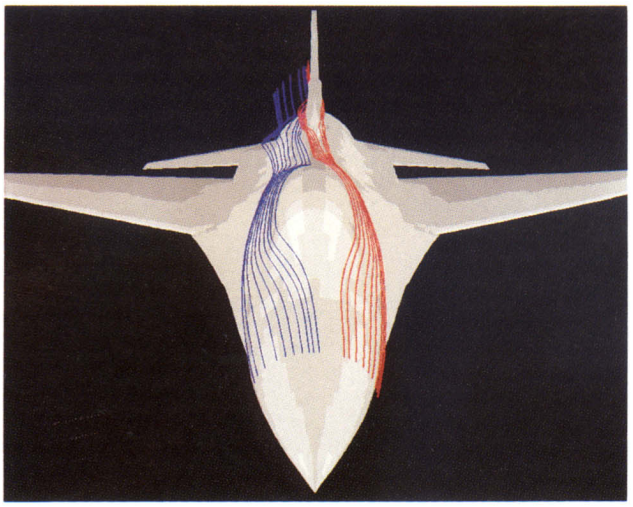

Fig. 13 Computed unrestricted particle traces for the F-16A in yaw with $M_\infty = 0.9$, $\alpha = 6.0$ deg, $\beta = 5.0$ deg, $Re = 4.5 \times 10^6$.

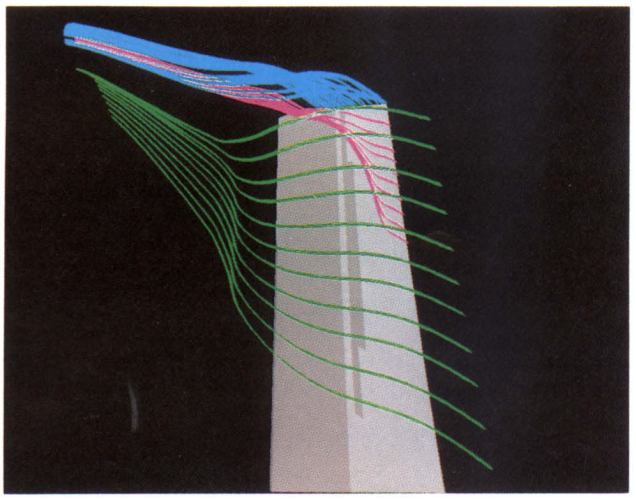

Fig. 14 Computed unrestricted particle traces for the vertical tail with $M_\infty = 0.9$, $\alpha = 6.0$ deg, $\beta = 5.0$ deg, $Re = 4.5 \times 10^6$.

past the leeward side of the vertical tail. The particle traces released from the windward side are also displaced by the canopy; however, some cross over the fuselage centerline and proceed along the leeward side of the vertical tail, while others proceed along the windward side.

Figure 14 illustrates unrestricted particle traces that are released near the leading edge and tip of the vertical tail. Traces in blue are released just outboard of the tip and indicate the formation of a tip vortex. The vortex rotation is not maintained farther downwind, however, due to insufficient grid resolution. A separation pattern appears near the leading edge, as indicated by the magenta traces. The traces converge along a separation line, are swept in a spanwise direction, and finally roll up into the tip vortex. Particles that are released further upstream of the leading edge, shown in green, proceed in a quasi-two-dimensional manner and then move slightly outboard due to a spanwise pressure gradient.

Conclusions

A zonal grid approach using the thin-layer, Reynolds-averaged Navier-Stokes equations has been successfully used to simulate transonic viscous flow about the F-16A fighter aircraft. The zonal approach was able to model this complex geometry with sufficient grid clustering near all body surfaces to capture viscous flow gradients. A typical average value of $y^+ = 3$ was obtained one grid point off the wing surface. A Mach number correction was needed to obtain good agreement between computational and experimental shock positions. The pressure suction peak on the wing leading edge was overpredicted. The experimental lift was underpredicted by 2.6%, and the experimental drag was overpredicted by 1.6%. The agreement of drag is somewhat fortuitous due to the lower induced drag. Overall, the comparisons were good; however, more grid refinement in body surface directions is warranted, especially near the wing leading edge and at shocks. The flexibility of the zonal method was demonstrated by adding additional grids inside the inlet up to the compressor face to create spillage and grids downwind of the exhaust nozzle to model power-on conditions. Computations for the F-16A in sideslip were also presented. These results indicated the proper trends, e.g., greater lift on the windward wing than the leeward wing. The results described above demonstrate that the present zonal Navier-Stokes approach is a flexible and viable means for simulating viscous flowfields about complex geometries.

Acknowledgments

The authors would like to thank Jason G. Williams of Sterling Software for his help in preparing the figures. The authors would also like to thank Reese L. Sorenson of NASA Ames Research Center for generating the coarse (nonzoned) grid about the F-16A fighter aircraft.

References

[1]Kutler, P., "A Perspective of Theoretical and Applied Computational Fluid Dynamics," AIAA Paper 83-0037, Jan. 1983.

[2]Ballhaus, W. F., "Supercomputing in Aerodynamics," Conf. on Frontiers of Supercomputing, Los Alamos, NM, 1983.

[3]Cosentino, G. B., and Holst, T. L., "Numerical Optimization Design of Advanced Transonic Wing Configurations," AIAA Paper 85-0424, Jan. 1985.

[4]MacCormack, R. W., "The Numerical Solution of the Compressible Viscous Flow Field about a Complete Aircraft in Flight," *Recent Advances in Numerical Methods in Fluids,* Vol. 3, edited by W. G. Habashi, Pineridge, 1984.

[5]Tinoco, E. N., Ball, D. N., and Rice II, F. A., "PAN AIR Analysis of a Transport High-Lift Configuration," AIAA Paper 86-1811, June 1986.

[6]Eberle, A., "Euler Solution for a Complete Fighter Aircraft Configuration at Sub- and Supersonic Speed," AGARD Paper 17, April 1986.

[7]Karman, S. L., Steinbrenner, J. P., and Kisielewski, K. M., "Analysis of the F-16 Flow Field by a Block Grid Euler Approach," AGARD Paper 18, April 1986.

[8]Peraire, J., Peiro, J., Formaggia, L., Morgan, K., and Zienkiewicz, O. C., "Finite Element Euler Computations in Three Dimensions," AIAA Paper 87-0032, Jan. 1987.

[9]Jameson, A., and Baker, T. J., "Improvements to the Aircraft Euler Method," AIAA Paper 87-0452, Jan. 1987.

[10]Yu, N. J., Kusunose, K., Chen, H. C., and Sommerfield, D. M., "Flow Simulations for a Complex Airplane Configuration Using Euler Equations," AIAA Paper 87-0454, Jan. 1987.

[11]Sawada, K., and Takanashi, S., "A Numerical Investigation on Wing/Nacelle Interferences of USB Configuration," AIAA Paper 87-0455, Jan. 1987.

[12]Szema, K. Y., Chakravarthy, S. R., Pan, D., and Bihari, B. L., "The Application of a Unified Marching Technique for Flow Over Complex 3-Dimensional Configurations Across The Mach Number Range," AIAA Paper 88-0276, Jan. 1988.

[13]Atta, E. H., "Component-Adaptive Grid Interfacing," AIAA Paper 81-0382, Jan. 1981.

[14]Atta, E. H., and Vadyak, J. A., "Grid Interfacing Zonal Algorithm for Three-Dimensional Transonic Flows about Aircraft Configurations," AIAA Paper 82-1017, June 1982.

[15]Hessenius, K. A., and Pulliam, T. H., "A Zonal Approach to Solution of the Euler Equations," AIAA Paper 82-0969, June 1982.

[16]Rai, M. M., "A Conservative Treatment of Zonal Boundaries for Euler Calculations," AIAA Paper 84-0164, Jan. 1984.

[17]Flores, J., Holst, T. L., Kaynak, N., Gundy, K., and Thomas, S. D., "Transonic Navier-Stokes Wing Solution Using a Zonal Approach: Part 1. Solution Methodology and Code Validation,"

AGARD Paper 30A, April 1986.
[18]Flores, J., Reznick, S. G., Holst, T. L., and Gundy, K., "Navier-Stokes Solutions for a Fighter-Like Configuration," AIAA Paper 87-0032, Jan. 1987.
[19]Flores, J., Chaderjian, N. M., and Sorenson, R. L., "Simulation of Transonic Viscous Flow over a Fighter-Like Configuration Including Inlet," AIAA Paper 87-1199, June 1987.
[20]Beam, R. M., and Warming, R. F., "An Implicit Finite-Difference Algorithm for Hyperbolic Systems in Conservation Law Form," *Journal of Computational Physics,* Vol. 22, No. 1, 1976, pp. 87-110.
[21]Pulliam, T. H., and Steger, J. L., "Implicit Finite Difference Simulations of Three-Dimensional Compressible Flow," *AIAA Journal,* Vol. 18, No. 2, 1980, p. 159-167.
[22]Pulliam, T. H., and Chaussee, D. S., "A Diagonal Form of An Implicit Approximate-Factorization Algorithm," *Journal of Computational Physics,* Vol. 39, No. 2, 1981, pp. 347-363.
[23]Pulliam, T. H., "Artificial Dissipation Models for the Euler Equations," AIAA Paper 85-0438, Jan. 1985.
[24]Baldwin, B. S., and Lomax, H., "Thin Layer Approximation and Algebraic Model for Separated Turbulent Flow," AIAA Paper No. 78-257, 1978.
[25]Shang, J. S., Hankey, W. L., and Petty, J. S., "Three-Dimensional Supersonic Interacting Turbulent Flow Along a Corner," AIAA Paper No. 78-1210, July 1978.
[26]Sorenson, R. L., "Three-Dimensional Elliptic Grid Generation About Fighter Aircraft for Zonal Finite-Difference Computations," AIAA Paper 86-0429, Jan. 1986.
[27]Reue, G. L., Doberenz, M. E., and Wilkins, D. D., "Component Aerodynamic Load from 1/9-Scale F-16A Loads Model," General Dynamics, Fort Worth, TX, Rept. 16PR316, May 1976.

Color reproduction courtesy of NASA Ames Research Center